Journal of Zhejiang University-SCIENCE A (Applied Physics & Engineering)
ISSN 1673-565X (Print); ISSN 1862-1775 (Online)
www.jzus.zju.edu.cn; www.springerlink.com
E-mail: jzus@zju.edu.cn

Calculation and experimental verification of radiation characteristics of spontaneous chaff clouds in high-speed flows*

Biao WANG†, He-song HUANG, Yong-jian YANG

Aeronautics Engineering College, Air Force Engineering University, Xi'an 710038, China

†E-mail: kbdbtgyd@sina.com

Received Jan. 17, 2019; Revision accepted Apr. 29, 2019; Crosschecked May 8, 2019

Abstract: When spontaneous chaffs diffuse in air, numerous radiations are shielded, absorbed, and reflected between chaffs, and there is interaction between the chaffs and the air. This makes it relatively complicated to calculate radiation transmission. To calculate the spatial distribution and generate radiation images of spontaneous chaffs, a radiation calculation model based on reverse path sampling was constructed which takes account of the transmission characteristics of radiation. This model hypothesizes that all detectors transmit light outward uniformly in the opposite direction of the radiation. After sampling statistics of light routes, the number and intensity of lights received by detectors along the radiation path were calculated. Next, a spontaneous combustion model of chaff was constructed. In this model, the effects of the porous structure of the chaff surface on the combustion rate of reactive metals are considered. The accuracy of this model was proved by comparing calculated results with experimental data. Finally, the spatial distribution of chaff clouds was calculated and their radiation images obtained. The results from the constructed model proved to be highly accurate when compared with measurement data from an experimental rocket sled.

Key words: Chaff clouds; Radiation calculation; Special radiance characteristics; Reactive metals; Spontaneous combustion
https://doi.org/10.1631/jzus.A1900020 **CLC number:** TJ761.1

1 Introduction

With the development of infrared countermeasure technology in air combat, a new generation of infrared decoys is represented by surface-type infrared decoys based on spontaneous metal chaffs (Viau et al., 2014; Lv, 2015; SAAB Technologies, 2017). Thousands of metal chaffs are ejected by the trigger mechanism at the release of infrared decoys. Chaffs diffuse in air and reactive metals coated on the chaffs combust spontaneously upon contact with oxygen, forming a radiation source in the air. This radiation source covers a certain area and presents a certain shape.

The main difficulties in studying the radiation characteristics of spontaneous chaff clouds formed after the release of decoys are as follows. (1) Chaff clouds diffuse at high altitude and high speed. The diffusion shape of chaff clouds is difficult to determine because it is influenced by the wake field of the aircraft. To address this problem, many researchers have carried out detailed studies and constructed diffusion models of chaffs under the driving effect of a jet stream (Denison and Hookham, 1996; Lin and Li, 2007; Li and Wang, 2009; Tong et al., 2015; Wang et al., 2015; Zou et al., 2016; Huang et al., 2018). (2) To expand the area of contact with air, chaffs have porous surface structures. Oxygen in air enters the chaff pores where it reacts with reactive metals. However, the reaction rate at high altitudes and changes in corresponding chaff temperature are difficult to determine. Many studies of the combustion characteristics of metals have been reported (Koch et al., 2011;

* Project supported by the National Natural Science Foundation of China (No. 61471390)
ORCID: Biao WANG, https://orcid.org/0000-0001-7007-7650

Gao et al., 2015; Liao et al., 2016; Wang et al., 2016), but few have discussed metal combustion behavior in porous media under a jet stream. (3) In spontaneous chaff clouds, there is mutual shielding, absorption, and reflection among thousands of chaffs, which makes the determination of the infrared radiation characteristics and the production of radiation images very difficult. Previous studies have covered the emission and shielding of decoys, but neglected mutual absorption and reflection in chaff clouds. (4) Spontaneous chaffs interact with air in the ambient environment. These interactions may involve heat exchange between chaffs and air, chaff radiation absorption by air, chaff radiation scattering in air, and radiated emission of air.

Results from some studies of the transmission of radiation in complicated shape structures have been applied. The transmission of radiation has been calculated using a global illumination algorithm (Coiro, 2013; Chang et al., 2015; Wu and Zhang, 2015; Wu et al., 2015). In addition to radiation received by an object surface from a light source, global illumination also has to calculate radiation reflected onto the object surface after interaction with other objects as well as the radiation emitted by the object. Previous global illumination algorithms have been based on Monte Carlo method, stochastic photon mapping, and point-based global illumination. Although these algorithms have high accuracy, they incur high calculation loads. Radiation transmission has been calculated using the reverse Monte Carlo method (Everson and Nelson, 1993; Gao et al., 2013; Chen et al., 2014; Lan et al., 2015). In this method, a beam path is tracked in reverse from the detector, thereby enabling the determination of the number of beams entering the detector along the radiation emission routes. This method is based mainly on the principle of reciprocity in radiation transmission, and reduces calculation loads effectively relative to the positive Monte Carlo method. However, the reverse Monte Carlo method is still based on statistical principles and has complicated calculations.

In this study, the combustion and radiation characteristics of spontaneous chaffs during diffusion in air were determined. Key attention was paid to the combustion characteristics of spontaneous metals in porous structures under a jet stream, the shielding, absorption, and reflection of radiations among chaffs, and the interaction between chaffs and air. A calculation model based on a detector was constructed to calculate the transmission of radiation. This model not only considers reflection, adsorption, emission, and shielding between chaffs and air, but also reduces calculation loads effectively. It was proved to be highly accurate by a static chaff combustion experiment and a dynamic experimental launch of a rocket sled emitting chaff clouds.

2 Radiation calculation model based on reverse path sampling

During the diffusion of chaff clouds in air, the infrared radiation characteristics of chaffs are obvious due to the high temperature caused by combustion in air. However, the transmission of radiation is complicated due to the great number of chaff clouds. Firstly, there is considerable radiation shielding, reflection, and absorption among different chaffs (Fig. 1). Several typical interaction modes of chaffs were introduced by considering four chaffs. Suppose that Chaff1 emits a photon, Photon1, which has a wavelength of λ. R1 is the transmission path of Photon1. R1 is reflected by Chaff2 and Chaff3 and finally arrives at the infrared detector. Since the chaff surfaces are rough, reflections of radiation do not obey the law of specular reflection. Similarly, R2 starts from Chaff1 and is absorbed by Chaff2 after it is transmitted to the Chaff2 surface. R3 starts from Chaff2 and enters the air after reflection by Chaff3, but does not arrive at the infrared detector. R4 starts from Chaff4, points to the detector, and locates in the field of view of the detector. However, shielded by Chaff3, R4 fails to enter the detector. Secondly, chaffs can interact with air. These interactions may include heat exchange between chaffs, absorption and diffusion of chaff radiation by air, and radiation emission of air. Heat exchange and radiation exchange between chaffs and the surrounding air are shown in Fig. 2. Similar to Fig. 1, suppose the chaff emits a photon, Photon1, which has a wavelength of λ. R1 is the transmission path of Photon1 which is finally absorbed by air at P1 after propagation for a certain period. R2 starts from the chaff and is diffused by air after propagation for a certain period. R3 and R4 are transmission paths of photons emitted through the

surrounding air to the outside. The surrounding air temperature is increased by heat absorption from chaff combustion, leading to more obvious infrared characteristics.

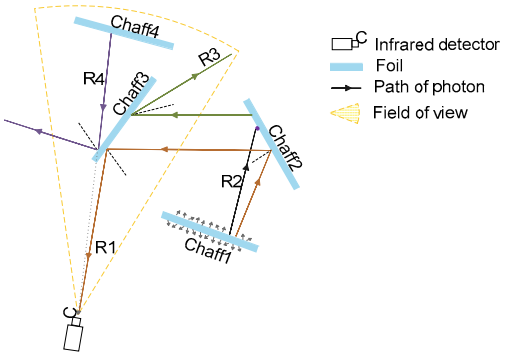

Fig. 1 Radiation shielding, reflection, and absorption among different chaffs

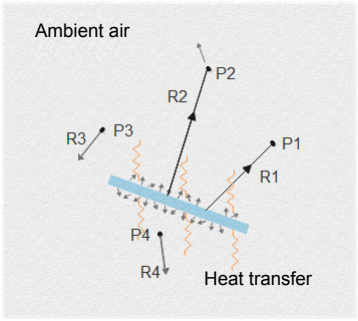

Fig. 2 Heat exchange and radiation exchange between chaffs and surrounding air

2.1 Method

In Fig. 1, only light rays which are in the field of view of the detector and which point to the detector can be sensed by the detector. For example, most lights of R2, R3, and R4 cannot enter the detector and can be neglected in calculation to save computation resources. Therefore, in theory, a global illumination algorithm can produce accurate infrared images of chaff clouds using positive statistics of the emission, absorption, reflection, and diffusion of each light and statistics of lights entering the infrared detector. However, that involves calculation of numerous unnecessary lights, thereby increasing computational complexity. To solve this problem, a radiation calculation model based on reverse path sampling was constructed. In this model, we firstly hypothesized that the detector sends lights outward uniformly at different angles in the opposite direction of the radiation. Secondly, the paths of each light are counted. Finally, the number and intensity of lights received by the detector in the direction of the radiation are calculated.

The calculation method used in this study is based on ray tracing (Appel, 1968; Whitted, 1979; Nebel, 1998; Nikodym, 2010). Ray tracing is a method for displaying objects (Appel, 1968). The method randomly emits and tracks light in its field of view. When light R intersects with the object at point P_0, n_0 lights of R reflected by P_0 can be obtained, and the n_0 lights can be continued to be tracked. The corresponding radiation intensity of each light is obtained through tracking, and then the corresponding relationship between the light direction and the pixel is established to obtain the infrared image. The algorithm in this study combines ray tracing with a sampling process based on reflection probability.

The basic principle of the proposed radiation calculation model based on reverse path sampling is introduced briefly in Fig. 3. In this case, the infrared detector sends three lights R1–R3 (intensity is I_d) in the field of view uniformly. R1 arrives at the Chaff2 surface after propagation in air. Some of R1 is absorbed by Chaff2 and the rest is reflected. According to the law of reflection, the directions of reflected lights distribute with a certain probability. The bidirectional reflectance distribution function (BRDF) model is used to describe such a probability (Geisler-Moroder and Dür, 2010; Yuan et al., 2010; Su et al., 2014; Wu, 2015):

$$f_{\mathrm{BRDF}}(\theta_{\mathrm{i}},\phi_{\mathrm{i}};\theta_{\mathrm{r}},\phi_{\mathrm{r}};\lambda)=\frac{\mathrm{d}L(\theta_{\mathrm{r}},\phi_{\mathrm{r}})}{\mathrm{d}E(\theta_{\mathrm{i}},\phi_{\mathrm{i}})}[\mathrm{sr}^{-1}], \tag{1}$$

where $L(\theta_{\mathrm{r}}, \phi_{\mathrm{r}})$ is the radiation intensity of the reflected light, $E(\theta_{\mathrm{i}}, \phi_{\mathrm{i}})$ is the radiation energy of the incident ray, θ_{i} and ϕ_{i} are the angle of pitch and the azimuth angle of the incidence light, and θ_{r} and ϕ_{r} are the angle of pitch and the azimuth angle of the reflected light, respectively. sr^{-1} is the unit, and sr is the steradian for solid angle.

The BRDF model has been studied extensively. In this study, the new Ward model was applied. The basic formula of the new Ward model is (Geisler-Moroder and Dür, 2010):

$$f_{\text{newWard}}=\frac{\rho_{\text{s}}}{\pi\alpha\beta}\exp\left[-\tan^2\delta\left(\frac{\cos^2\phi_{\text{h}}}{\alpha^2}+\frac{\sin^2\phi_{\text{h}}}{\beta^2}\right)\right]\times\frac{2\left[1+\cos\theta_{\text{i}}\cos\theta_{\text{r}}+\sin\theta_{\text{i}}\sin\theta_{\text{r}}\cos(\phi_{\text{r}}-\phi_{\text{i}})\right]}{(\cos\theta_{\text{i}}+\cos\theta_{\text{r}})^4}. \quad (2)$$

The parameters in this formula and the reflection characteristics of chaffs calculated in this formula are shown in Appendix A.

Since reflected lights occupy the whole space and cannot be calculated completely, some sampling directions were chosen according to the new Ward probability, and a total of N_{r} reflected lights were collected. Hence, N_{r} light transmission paths from R1 can be gained (Rf1–Rf4 in Fig. 3). These N_{r} light transmission paths distribute according to the new Ward probability. Next, radiation arriving at the infrared detector along R1 was calculated along the opposite directions of these N_{r} light transmission paths.

The radiation calculation was introduced based on R1-Rf1, as follows. Since Rf1 points to air, radiation received by chaffs through R1-Rf1 is the sum of the radiation emitted by Chaff2, radiation from Rf1, and radiation reflected by Chaff2. Therefore, the radiation intensity on Rf1 is

$$L_{\text{R1-Rf1}}=\tau_{\text{R1-air}}[L_{\text{n2}}\cos\theta_{\text{R1}}+L_{\text{Rf1}}(1-\rho_{\text{f}})]+L_{\text{R1-air}}, \quad (3)$$

where $L_{\text{n}i}$ is the radiation intensity of Chaff$i$ along the normal direction, θ_{R1} is the normal included angle between R1 and Chaff2, L_{Rf1} is the air radiation intensity along Rf1, ρ_{f} is the absorption rate of chaffs, and $\tau_{\text{R1-air}}$ and $L_{\text{R1-air}}$ are transmittances on R1 and the radiation intensity of air, respectively. Due to sampling based on the new Ward probability, differences in the reflectivity of chaffs along different reflection directions are neglected in calculating all N_{r} transmission paths derived from R1. Therefore, the total radiation intensity along R1 is

$$L_{\text{R1}}=\frac{1}{N_{\text{r}}}\sum_{i=1}^{N_{\text{r}}}L_{\text{R1-Rf}i}. \quad (4)$$

Since there are N_{r} transmission paths along R1, we obtain

$$L_{\text{R1}}=\frac{1}{N_{\text{r}}}\sum_{i=1}^{N_{\text{r}}}L_{\text{Rf}i}(1-\rho_{\text{f}})+\tau_{\text{R1-air}}L_{\text{n2}}\cos\theta_{\text{R1}}+L_{\text{R1-air}}. \quad (5)$$

This is the calculation formula of radiation on Rf1. Note that the above cases all hypothesized Rf1–Rf4 entering into air. Therefore, $L_{\text{Rf}i}$ is the atmospheric radiation from Rfi, which may still have intersections with chaffs (Rf5 in Fig. 3). Therefore, $L_{\text{Rf}i}$ should be understood as the sum of chaff radiation from Rfi and air radiation. Theoretically, calculation of radiation along Rf5 is the same as that of Rf1 (Eq. (6)). However, the radiation intensity of Rf5 is decreased significantly after one reflection, and the light intensity for the second reflection by Chaff1 is very low. As a result, the secondary or subsequent reflections are neglected. In this way, the radiation intensity along Rf5 can be calculated by

$$L_{\text{Rf5}}=\tau_{\text{Rf5-air}}L_{\text{n1}}\cos\theta_{\text{Rf5}}+L_{\text{Rf5-air}}. \quad (6)$$

Parameters in this formula are similar to those in Eq. (5).

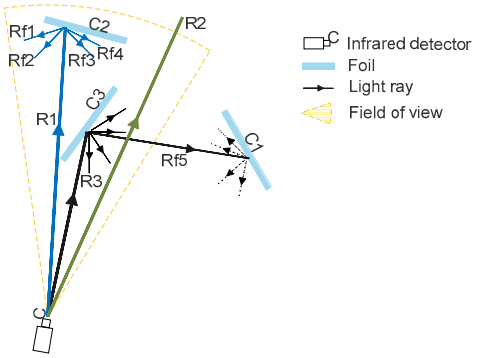

Fig. 3 Basic principle of the reverse path sampling radiation calculation model

If the infrared detector sends N_{d} lights R_{i} into its field of view uniformly, the radiation intensity of these N_{d} lights can be calculated from Eq. (5). On this basis, the infrared image of the scene in the field of view of the infrared detector can be obtained.

2.2 Line of sight

Infrared radiation which is emitted by the target enters the optical system of the infrared detector after propagation in air and is then reflected by the optical system, imaging on the focal plane of the detector.

The range of the field of view of the infrared detector is shown in Fig. 4, where $\theta_1 \times \theta_2$ is the angle of the field of view of the detector. For single pixel points on the focal plane, the received radiation range is actually a cone with a certain angle (shaded area in Fig. 4). For a specific infrared optical system, the cone of sight corresponding to each pixel point is fixed after the field of view is determined. If the optical distortion effect of the imaging system is neglected, the cone of sight corresponding to each pixel point distributes uniformly in the field of view of the detector.

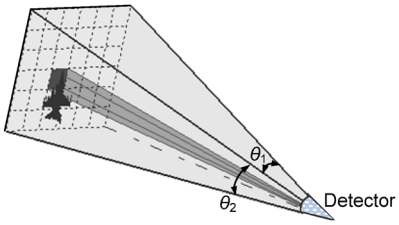

Fig. 4 Range of the view field of the infrared detector

A coordinate system ($O_DX_DY_DZ_D$) of the detector is constructed to describe the cone of sight and sight equation corresponding to each pixel point. In Fig. 5, O_D is at the center of the focal plane array. Axis O_DX_D points in the normal direction of the focal plane of the detector. Axis O_DY_D is in the focal plane of the detector and is parallel to the bottom line of the focal plane array. Axis O_DZ_D is also in the focal plane and is parallel with the other side of the focal plane array. Axis O_DZ_D forms the right-handed coordinate system with the O_DX_D and O_DY_D axes. In the coordinate system of the detector, the midline equation of the cone of sight for pixel points at $(0, y_1, z_1)$ can be described as

$$\begin{cases} xy_1 \tan\dfrac{\theta_1 y_1}{2y_m} = y - y_1, \\ xz_1 \tan\dfrac{\theta_2 z_1}{2z_m} = z - z_1, \end{cases} \tag{7}$$

where y_m and z_m are the maximum y and z values, respectively, of the focal plane array in the focal plane coordinate system. The deduction process of this equation is shown in Appendix B. If the pixel number of the focal plane array is $M_1 \times M_2$, the angle of the cone of sight corresponding to each pixel point is $(\theta_1/M_1)\times(\theta_2/M_2)$. Therefore, the equation that covers all lines in this cone of sight can be expressed as:

$$\begin{cases} xy_1 \tan\theta_y = y - y_1, \\ xz_1 \tan\theta_z = z - z_1, \end{cases} \tag{8}$$

$$\theta_y \in \left[\frac{\theta_1 y_1}{2y_m} - \frac{\theta_1}{2M_1}, \frac{\theta_1 y_1}{2y_m} + \frac{\theta_1}{2M_1}\right], \tag{9}$$

$$\theta_z \in \left[\frac{\theta_2 z_1}{2z_m} - \frac{\theta_2}{2M_2}, \frac{\theta_2 z_1}{2z_m} + \frac{\theta_2}{2M_2}\right]. \tag{10}$$

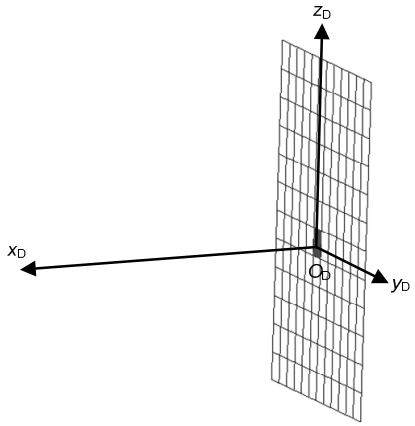

Fig. 5 Schematic diagram of the detector coordinate system

When solving the infrared image produced by the detector, a brightness matrix must first be defined to record infrared radiation intensity received by each pixel point. Later, the infrared radiation intensity received by each pixel point is calculated and results are stored in the brightness matrix. Finally, brightness values in the matrix are quantized into grey values to produce an infrared image. Firstly, N_p lines in a uniform distribution are produced according to Eq. (8). Subsequently, the infrared radiation intensity received by each pixel point is calculated from Eq. (5). The brightness mean of N_p lines is used as the infrared radiation intensity received by this pixel point.

Locations of the detector and target object are generally given in terms of the earth coordinate system. For convenience of calculation, these coordinates have to be transformed into the detector coordinate system. Suppose that the coordinates of the detector and target are (x_D, y_D, z_D) and (x_P, y_P, z_P),

respectively, in the earth coordinate system, the unit vector of the detector normal in the earth coordinate system is (n_{x1}, n_{x2}, n_{x3}), and the unit vector of the y-axis of the detector coordinate system in the earth coordinate system is (n_{y1}, n_{y2}, n_{y3}). Then, the coordinates of the target aircraft in the detector coordinate system (x_w, y_w, z_w) can be calculated by

$$\begin{cases} x_w = (x_P - x_D)n_{x1} + (y_P - y_D)n_{x2} + (z_P - z_D)n_{x3}, \\ y_w = (x_P - x_D)n_{y1} + (y_P - y_D)n_{y2} + (z_P - z_D)n_{y3}, \\ z_w = \sqrt{(x_P - x_D)^2 + (y_P - y_D)^2 + (z_P - z_D)^2 - x_w^2 - y_w^2}. \end{cases} \tag{11}$$

3 Combustion model of spontaneous chaff and experimental verification

3.1 Combustion model of spontaneous chaff

In this section, a combustion model of chaff is established to calculate the change of chaff temperature with time t. A surface-type infrared decoy usually adopts a surface porous structure to increase the contact area between a pyrophoric substance, composed mainly of magnesium, and oxygen. If the heat conduction inside the metal is ignored, the energy change of the chaff is equal to the sum of the energy generated by combustion, the heat convection with air, and the heat emitted by thermal radiation. The formula for calculation of the chaff's energy change is

$$\frac{\partial Q_{\text{chaff}}}{\partial t} = \frac{\partial Q_{\text{Mg}}}{\partial t} - \frac{\partial Q_{\text{con}}}{\partial t} - \frac{\partial Q_{\text{rad}}}{\partial t}, \tag{12}$$

where Q_{chaff} is the total heat of the chaff, Q_{Mg} is the heat generated by combustion, Q_{con} is the heat convection with air, and Q_{rad} is the heat emitted by thermal radiation. According to Stefan-Boltzmann's law, Q_{rad} is proportional to temperature to the fourth power.

$$\frac{\partial Q_{\text{rad}}}{\partial t} = A\sigma\varepsilon(T^4 - T_a^4), \tag{13}$$

where A is the superficial area of chaff, σ= 5.67×10^{-8} W/(m^{2}K^4) is the Stefan-Boltzmann constant, ε is the emissivity of chaff, T is the temperature of the chaff, and T_a is the temperature of the air.

Due to the large diffusion area of the chaff cloud, there is hardly any direct contact between the chaffs, but there is still heat exchange between them. Heat exchange occurs in two main ways: one is heat transfer between chaffs, with air as the conduction medium, which occurs mainly between chaffs and air; the other is the heat exchange between chaffs through heat radiation. However, due to the large diffusion area of the chaff cloud, the temperature change caused by these two factors is very small and can be ignored.

As the chaff is flying, the surrounding air is driven to move because of its viscosity, which produces internal friction in air. This internal fraction heats the surrounding air. The heat convection with air can be described as

$$\frac{\partial Q_{\text{con}}}{\partial t} = Ah_x(T - T_a), \tag{14}$$

where h_x is the convection heat transfer coefficient, and h_x can be calculated from (Bennett and Myers, 1982)

$$h_x = 0.332\sqrt{\frac{\rho V_f}{D_f}}\sqrt[6]{\frac{c_p^2\lambda_a^4}{\mu}}. \tag{15}$$

where ρ is the air density, V_f is the velocity of chaff, D_f is the diameter of chaff, c_p is the constant pressure specific heat of air, λ_a is the heat conduction coefficient, and μ is the dynamic viscosity coefficient of air.

The chaff that makes up the surface-type decoy consists of an inert base and a pyrophoric substance. A surface porous structure is usually adopted to increase the contact area between the pyrophoric substance and air. A sketch of activated material chaff is shown in Fig. 6. Suppose the thickness of pyrophoric substance is L and the number of pores in the surface porous structure is n.

Experimental analysis shows that the spontaneous combustion rate of active metal (Mg) is related mainly to the environment temperature T_a, oxygen concentration C, chaff velocity V_f, and porosity ω. First, calculate the porosity of the active metal:

$$\omega = \frac{nD_h^2}{D_f^2}, \tag{16}$$

where D_h is the pore diameter. Assuming that the active metal and oxygen react uniformly on the surface of the foil, when the total consumption volume of oxygen at time t is $W_{O_2}(t)$, the consumption of active metal (Mg) is $kW_{O_2}(t)$, where k is the consumption ratio of Mg and O_2. Suppose the thickness of the pyrophoric substance at time t is $L(t)$, which can be calculated from

$$L(t) = L - \frac{LkW_{O_2}(t)M_{Mg}}{m}, \tag{17}$$

where m is the mass of Mg, and M_{Mg} is the molar mass of Mg.

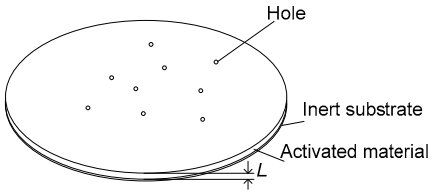

Fig. 6 Sketch map of activated material chaff

Oxygen in the air reacts with the active metal by diffusing into the porous structure. The diffusion includes volume diffusion and volume mass exchange. As the diameter of the pore is of the same order of magnitude as the mean free path of molecular diffusion, the oxygen molecules keep colliding with the pore wall in the process of diffusion. This makes the volume diffusion coefficient very small, and the diffusion resistance of oxygen in the pore very high. Therefore, the concentration of oxygen drops as the diffusion goes deeper, which reduces the reaction speed of spontaneous combustion.

The mass flow rate of O_2 per unit area is (Yan and Fan, 2016)

$$J_{O_2} = -D\frac{dC}{dz}, \tag{18}$$

where D is the diffusion coefficient of O_2, which can be calculated from

$$D = \frac{1}{6}D_h\left(\frac{RT}{\pi}\right)^{\frac{1}{2}}, \tag{19}$$

where R is the gas constant.

The active metal generates an amount of heat by reacting with oxygen. Meanwhile, its own weight keeps decreasing. Thus, there must be an equilibrium relationship between energy and mass, which is related to the oxygen concentration and active metal's temperature. The equilibrium of oxygen can be described as (Wilharm, 2003)

$$\omega\frac{dC}{dt} = D\frac{\partial^2 C}{\partial z^2} - \frac{4nD_h}{D_f^2}k_s C(z), \tag{20}$$

where k_s is the reaction rate constant, and $C(z)$ is the oxygen concentration at a depth of z, where $z=L(t)$ represents the surface of the active metal and $z=0$ represents the bottom of the active metal.

Suppose oxygen in the pore reaches the equilibrium point rapidly, then

$$\frac{dC}{dt} = 0. \tag{21}$$

Combining Eqs. (20) and (21) gives

$$\frac{d^2C}{dz^2} = \frac{4nD_h k_s C(z)}{D_f^2 D}. \tag{22}$$

At the bottom of the active metal ($z=0$), the oxygen concentration and the reaction rate are both the lowest, and there is almost no oxygen flowing in, so one of the boundary conditions is

$$\frac{dC}{dz}\Big|_{z=0} = 0. \tag{23}$$

At the surface of the active metal ($z=L(t)$), the oxygen concentration and the reaction rate are both the highest. Oxygen flows into the pore by volume diffusion and volume mass exchange. Thus, the other boundary condition is

$$D\frac{dC}{dz}\Big|_{z=L} = k_m\left(C_{O_2} - C(z)\right), \tag{24}$$

where C_{O_2} is the oxygen concentration in the environment. k_m is the volume mass exchange coefficient,

which can be calculated from (Bennett and Myers, 1982)

$$\begin{cases} k_{\mathrm{x}} = 0.182\left(\dfrac{p_0}{p}\right)\left(\dfrac{T}{T_0}\right)^{1.81}, \\ k_{\mathrm{m}} = 0.664\sqrt{\dfrac{V_{\mathrm{f}}}{D_{\mathrm{f}}}}\sqrt[6]{\dfrac{\rho k_{\mathrm{x}}^4}{\mu}}, \end{cases} \tag{25}$$

where p_0 is the standard atmospheric pressure, and T_0 is the standard atmospheric temperature.

By integrating Eq. (22) with boundary conditions Eqs. (23) and (24), the oxygen concentration at a depth of z is

$$C(z) = \frac{C_{\mathrm{O_2}}\cosh(\theta z)}{\cosh\left(L(t)\theta\right) + \dfrac{D\theta}{k_{\mathrm{m}}}\sinh\left(L(t)\theta\right)}, \tag{26}$$

where

$$\theta = \frac{2\sqrt{6nk_{\mathrm{s}}}}{D_{\mathrm{f}}}\left(\frac{RT}{\pi}\right)^{-\frac{1}{4}}, \tag{27}$$

$$D\frac{\mathrm{d}C}{\mathrm{d}z} = \int_0^{L(t)} \frac{4nD_{\mathrm{h}}k_{\mathrm{s}}C(z)}{D_{\mathrm{f}}^2}\mathrm{d}z. \tag{28}$$

The heat generated by combustion Q_{Mg} is

$$Q_{\mathrm{Mg}} = \Delta H J_{\mathrm{O_2}} S, \tag{29}$$

where ΔH is the reaction enthalpy of Mg combustion, and S is the pore area:

$$S = nL(t)\pi D_{\mathrm{h}}. \tag{30}$$

Based on the above analysis, the heat balance equation of chaff can be expanded as

$$\frac{c_{\mathrm{p}}mL(t)}{L}\frac{\partial T}{\partial t} = nL(t)\pi D_{\mathrm{h}}\int_0^{L(t)}\frac{4\Delta H D_{\mathrm{h}}k_{\mathrm{s}}nC(z)}{D_{\mathrm{f}}^2}\mathrm{d}z - Ah_{\mathrm{x}}\left(T - T_{\mathrm{a}}\right) - A\sigma\varepsilon(T^4 - T_{\mathrm{a}}^4). \tag{31}$$

The consumption of oxygen can be calculated from

$$\frac{\partial W_{\mathrm{O_2}}}{\partial t} = 4nL(t)\pi D_{\mathrm{h}}\int_0^{L(t)}\frac{D_{\mathrm{h}}k_{\mathrm{s}}nC(z)}{D_{\mathrm{f}}^2}\mathrm{d}z. \tag{32}$$

3.2 Simulation calculation and experimental verification

The above combustion model was applied to calculate the temperature change curve of chaffs. The values of parameters are shown in Table 1.

Fig. 7 shows the calculated temperature curve. The abscissa is the duration of combustion of the chaff, and the ordinate is the combustion temperature.

Table 1 Value of each parameter in the chaff temperature calculation

Parameter	Value
Pore diameter, D_{h} (m)	1.24×10^{-6}
Chaff diameter, D_{f} (m)	0.0465
Rate constant, k_{s} (cm/s)	0.03
Emissivity, ε	0.85
Activated metal weight, m (g)	0.6

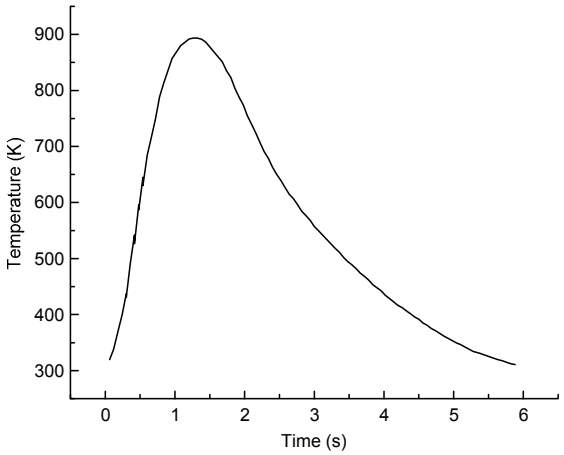

Fig. 7 Calculated combustion temperature curve

The temperature climbs quickly after chaff combustion begins, reaching the maximum (893 K) at about 1.3 s. Subsequently, the temperature drops slowly, decreasing to room temperature after about 6.0 s.

The accuracy of the radiation calculation model based on reverse path sampling was verified by a chaff static combustion experiment. The combustion temperature of the reactive metals was tested using an

SC7700MW thermal infrared imager with a working waveband of 3–5 μm and a field of view of 11.0°×8.8°. Reactive metal chaffs faced the thermal infrared imager directly from a distance of 10 m. The parameters of all chaffs used in the experiment were the same as those listed in Table 1. The thermal infrared images of reactive metals at 1.5 s measured by the imager are shown in Fig. 8. Chaff temperatures at different times, calculated from radiation intensity measured by the thermal infrared imager, are shown in Fig. 9. The percentage error between the test temperature and the calculated temperature is shown in Fig. 10. The error between the calculated result and the measured result was controlled within a certain range, and the main error occurred in the rising temperature stage and the high temperature stage.

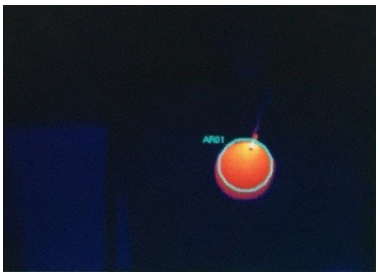

Fig. 8 Thermal infrared images of reactive metals at 1.5 s

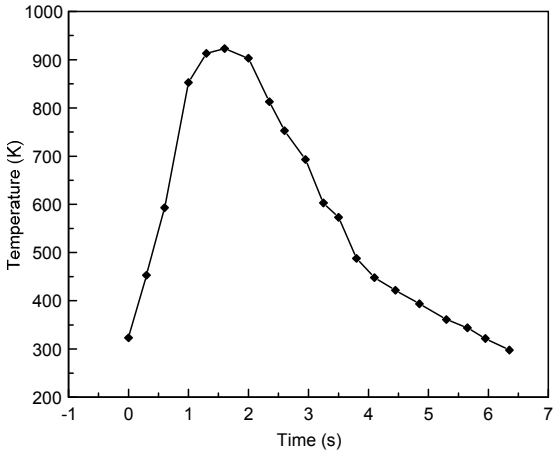

Fig. 9 Tested chaff temperatures at different times

3.3 Calculation of air temperature surrounding chaffs

A spatial dispersion algorithm based on finite volume, and a linear interpolation algorithm based on spatial second-order accuracy, were applied. The time discretization was accomplished by the backward difference method of second-order accuracy. Inlet, outlet, and outer walls of the calculation domain were all set far from the field of pressure. The chaff surface was assumed to have slippage-free walls, and the shear-stress-transport (SST) turbulence model was used (Huang et al., 2018). Since round chaffs have no sideslip angle, the ambient temperature field when the angle of attack of chaffs was 0°–90° was calculated by the computational fluid dynamics (CFD) algorithm at a step length of 5°. Based on calculation results, a temperature field database was formed. The temperature field projections of the lateral and front views of chaffs when the angle of attack was 30° are shown in Figs. 11 and 12, respectively.

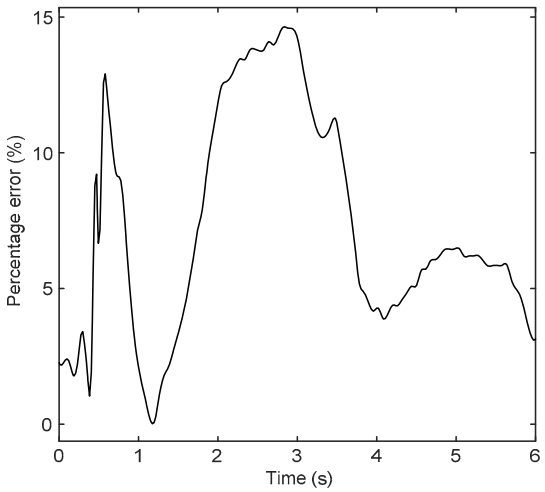

Fig. 10 Curve showing the error between the measured and the calculated temperatures

4 Radiation calculation of chaff clouds and experimental verification

4.1 Experimental methods and results

The validity of the model was verified by an experimental launch of a surface-type infrared decoy rocket sled. The diffusion laws of chaff clouds were tested using an FLIR SC3000 thermal infrared imager and an FTIR MR304 infrared spectrometer. The parameters of these two test machines are listed in Table 2 (p.468). The experiment layout is shown in

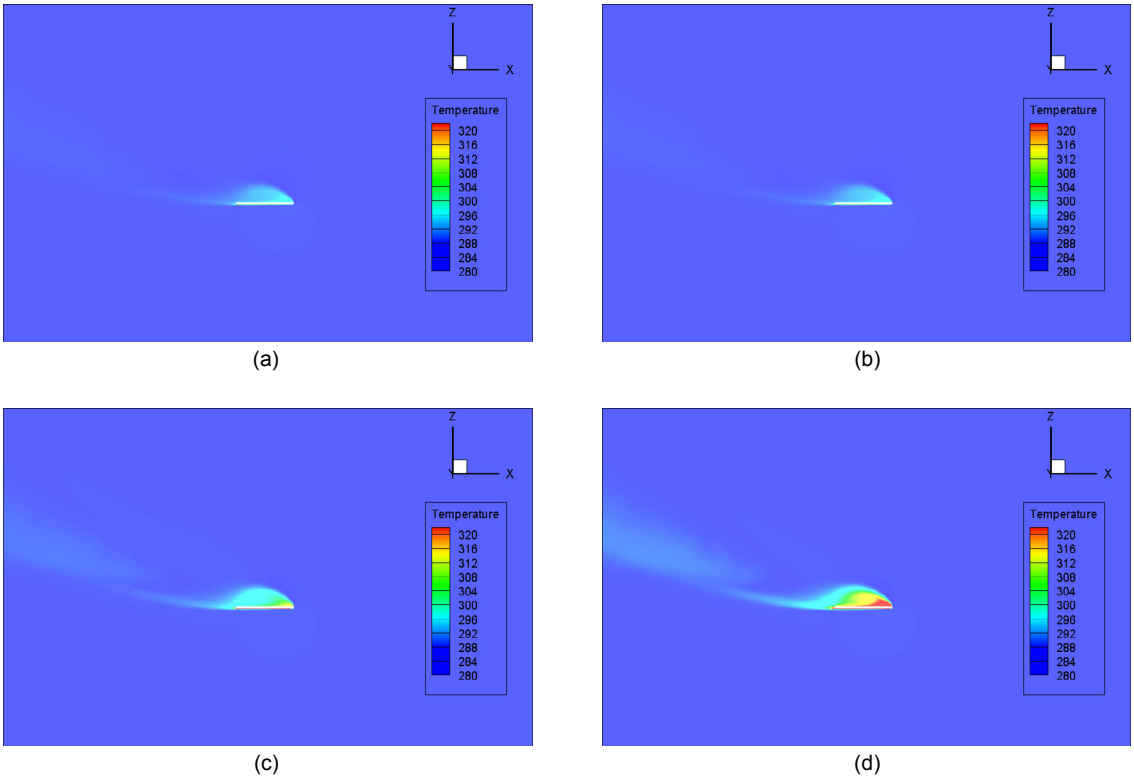

Fig. 11 Temperature field (unit: K) projections of the lateral view at different times: (a) 0.2 s; (b) 0.5 s; (c)1.0 s; (d) 1.5 s

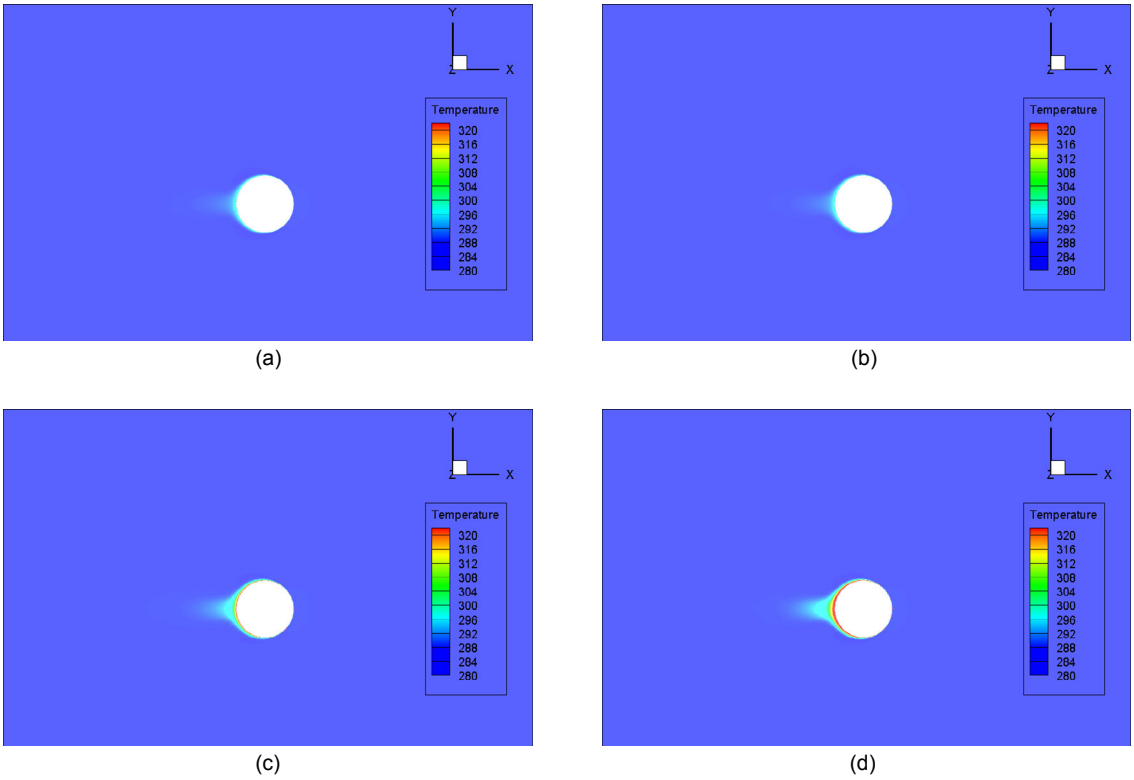

Fig. 12 Temperature field (unit: K) projections of the front view at different times: (a) 0.2 s; (b) 0.5 s; (c)1.0 s; (d) 1.5 s

Fig. 13. A total of 1000 chaffs were compressed horizontally and loaded into the launch tubes in a packet of infrared decoy. There were three launch tubes in the rocket sled, each installed with one packet of interference loads. Launch tubes were installed vertically on the rocket sled, and the launch speed was 25 m/s. Chaffs were coated with spontaneous reactive magnesium (Mg). Without physical cohesion between chaffs, all chaffs diffuse after the launch and combust spontaneously in air. The effects of the reaction heats produced by spontaneous combustion of chaffs on chaff diffusion can be neglected. In this way, infrared images of chaff clouds can be gained by the thermal infrared imager and the spectral characteristics of chaff clouds can be tested by the infrared spectrometer. The rocket sled ran in a horizontal orbit, 3 km long. Two test machines were located 194 m and 300 m, respectively, away from the orbit. The included angles between the central line of the fields of view of these two test machines and the positive side of the orbit were 0° and 53.1°, respectively. The rocket sled was ignited at the rightmost side of the orbit and launched the interference loads at a speed of 0.6 Ma (Mach) when it ran to the center of the field of view, 1100 m away.

Images of partial chaff clouds captured by the SC3000 thermal infrared imager are shown in Fig. 14.

The spectral characteristics of chaff clouds tested by the MR304 infrared spectrometer at 1.5 s are displayed in Fig. 15. When calculating the spectrum, the background radiation is removed, but since the atmospheric attenuation on the chaff cloud radiation transmission path cannot be ignored, the figure shows the spectrum of the chaff cloud after attenuation by the atmosphere.

Table 2 Parameters and relative locations of infrared radiation thermal imagers

Parameter	Description	
	MR304	SC3000
Type	Thermal infrared imager	Infrared spectrometer
Field of view	75 mrad	20°×15°
Test angle	53.1°	0°
Distance between imager and test region	300 m	194 m

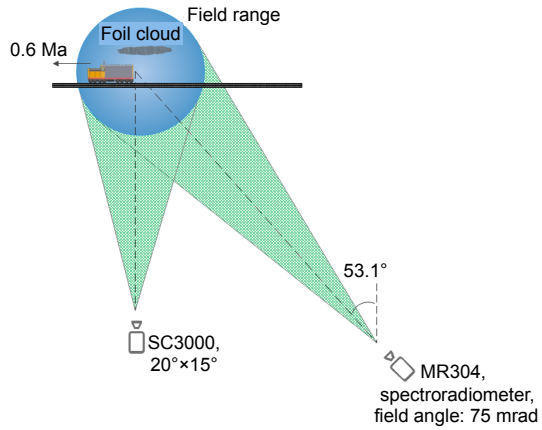

Fig. 13 Experimental schematic

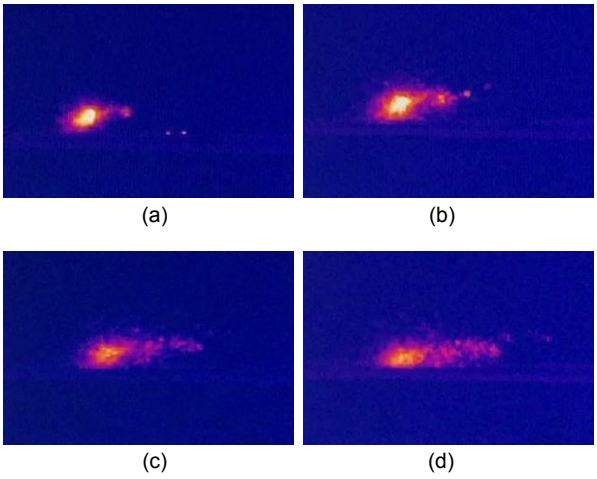

Fig. 14 Images of chaff clouds captured by the SC3000 thermal infrared imager at different times: (a) 0.5 s; (b) 1.0 s; (c) 1.5 s; (d) 2.0 s

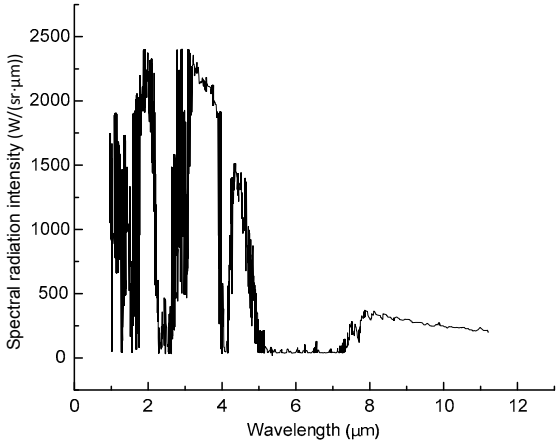

Fig. 15 Spectral characteristics of chaff clouds tested by the MR304 infrared spectrometer

Based on the images obtained, the chaff clouds were oval in shape during the diffusion process. The diffusion area expanded gradually as time went on. The brightness first increased and then decreased, while the brightness center gradually shifted backwards. The spectra of the chaff clouds reached maximal points at 2.0, 3.1, 4.3, and 8.0 μm (Fig. 15). They fluctuated mostly at 1.0–1.5 μm and the maximum peak was observed at about 3.1 μm. The maximum spectral radiation intensity was about I_{max}= 2363.8 W/(sr·μm).

4.2 Simulation calculation results and error analysis

Given the same conditions as those in the experiment, the radiation of the chaff cloud formed by 1000 pieces of spontaneous chaffs was calculated by combining the radiation calculation model and the chaff combustion model. Since this study focused on modeling the radiation characteristics of chaff clouds, a diffusion model of a chaff cloud was not established. Instead, the diffusion model established by Huang et al. (2018) was adopted. The grey infrared images of the calculated chaff cloud are shown in Fig. 16. The rule of Sun and Wang (2017) is used to convert infrared radiance into gray value.

Some parameters gained from analysis of the above images are listed in Table 3. The total pixel number of the four images was 300×200.

The infrared spectral characteristics of the chaff cloud at 1.5 s are shown in Fig. 17. To simulate the conditions consistent with Fig. 15, the background radiation was not calculated, and only the spectral radiation characteristics of the chaff cloud through atmospheric attenuation were calculated.

Fig. 16 and Table 3 show that the chaff cloud in the simulation presented a long elliptical diffusion

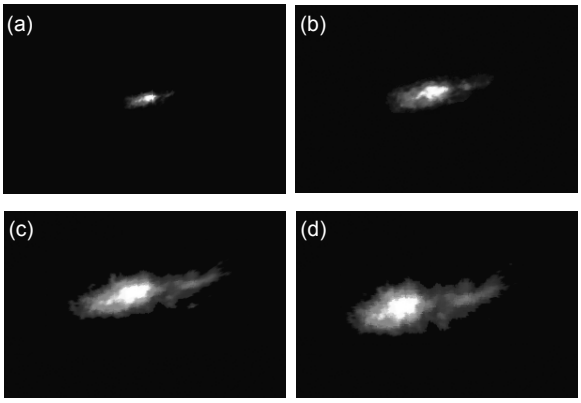

Fig. 16 Grey infrared images of the calculated chaff cloud at different times: (a) 0.5 s; (b) 1.0 s; (c) 1.5 s; (d) 2.0 s

Table 3 Some parameters of the calculated chaff cloud

Parameter	Description of parameter	Value			
		0.5 s	1.0 s	1.5 s	2.0 s
Area (pixel)	Pixel occupied by the main body of the chaff cloud	95	375	1385	1627
Bounding box (pixel)	Pixel of the minimum rectangle enclosing the main body of the chaff cloud	19×8	39×17	68×33	62×40
Major axis length (pixel)	Length of the long axe	19.10	34.86	68.08	61.97
Minor axis length (pixel)	Length of the short axe	6.94	14.81	26.57	34.34
Perimeter (pixel)	Perimeter of the main body of the chaff cloud	45.33	92.73	172.80	186.84
Physical size (m)	Actual size of the outer rectangle of the chaff cloud	15.2×7.2×5.7	35.1×15.3×12.2	55.1×29.7×25.4	56.8×36.5×30.3
Maximum infrared radiance (W/(sr·m^2))	Maximum brightness of the chaffs	12.29	38.68	53.20	47.35

pattern. The diffusion area expanded gradually with time and the center of brightness shifted backwards. According to the maximum infrared radiance data (Table 3), the maximum value was achieved at 1.5 s. The spectra of the chaff cloud developed maximal points at 1.4, 1.9, 3.1, 4.3, and 8.0 μm (Fig. 17). The peak was achieved at about 3.1 μm and the maximum spectral radiation intensity was I_{max}=2418.5 W/(sr·μm).

A comparison between the experimental results and the calculation results of spectral radiation intensity is shown in Fig. 18. The error curve is shown in Fig. 19. Obviously, the general trend of the simulation results conforms to that of the test results, showing high agreement in the middle and long wavebands. Error in the short waveband was caused mainly by the poor ability of the simulation to reflect high-frequency fluctuation in the measurement results. The maximum error point was at 4 μm. Since the wavelength range of these errors was small, they had little effect on the overall results. Based on the integration of spectral radiation intensity, the total radiation intensity gained from the experiment of the 1–11 μm waveband was I_{test}=6055.8 W/sr, whereas the total radiation intensity gained from the simulation was $I_{calculation}$=6628.2 W/sr.

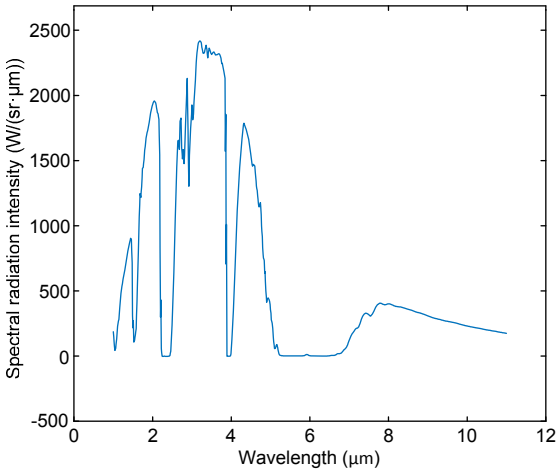

Fig. 17 Grey infrared images of the calculated chaff cloud

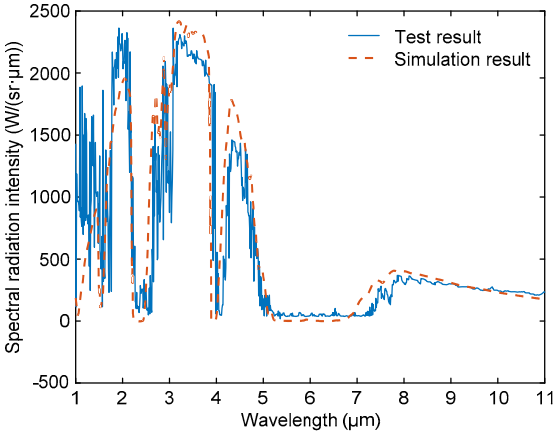

Fig. 18 Comparison between experimental and calculation results of spectral radiation

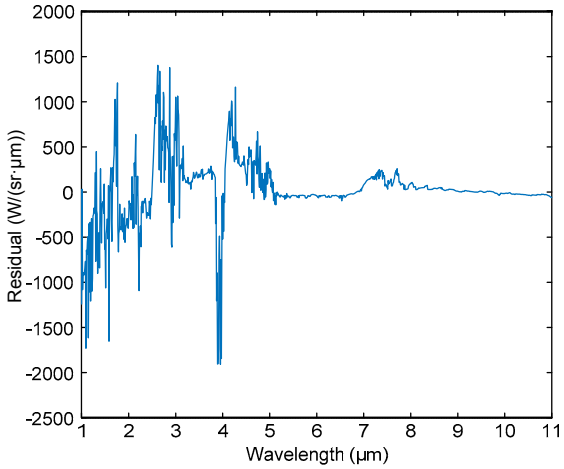

Fig. 19 Error curve between experimental and calculation results

5 Conclusions

In this study, the combustion and radiation characteristics of numerous spontaneous metal chaffs during diffusion in air were analyzed. A radiation calculation model and a combustion model were constructed, through which the radiation images and spectral characteristic curves of a spontaneous chaff cloud were obtained. These radiation images and spectral characteristics were compared with experimental results. Some major conclusions could be drawn:

1. The temperature climbed quickly after the combustion of chaffs and reached the maximum at about 1.3 s. Subsequently, the temperature dropped slowly and decreased to room temperature at about 6.0 s.

2. The chaff cloud presented a long elliptical diffusion pattern. The diffusion area expanded

gradually with time and the center of brightness shifted backwards.

3. The spectra of the chaff cloud developed maximal points at 1.4, 1.9, 3.1, 4.3, and 8.0 μm. The peak was achieved at about 3.1 μm and the maximum spectral radiation intensity was I_{max}=2418.5 W/(sr·μm).

4. The maximum total radiation intensity gained from the simulation of the 1–11 μm waveband was $I_{calculation}$=6628.2 W/sr.

References

Appel A, 1968. Some techniques for shading machine renderings of solids. Spring Joint Computer Conference, p.37-45. https://doi.org/10.1145/1468075.1468082

Bennett CO, Myers JE, 1982. Momentum, Heat, and Mass Transfer. McGraw-Hill, New York, USA, p.341.

Chang B, Park S, Ihm I, 2015. Diffuse global illumination in particle spaces. *Multimedia Tools and Applications*, 74(13):4987-5006. https://doi.org/10.1007/s11042-014-2132-x

Chen SG, Chen LH, Mo DL, et al., 2014. IR imaging simulation and analysis for aeroengine exhaust system based on reverse Monte Carlo method. International Symposium on Optoelectronic Technology and Application: Infrared Technology and Applications, Article 93000M. https://doi.org/10.1117/12.2070850

Coiro E, 2013. Global illumination technique for aircraft infrared signature calculations. *Journal of Aircraft*, 50(1): 103-113. https://doi.org/10.2514/1.C031787

Denison MR, Hookham PA, 1996. Modeling of dust entrainment by high-speed airflow. *AIAA Journal*, 34(7):1392-1402. https://doi.org/10.2514/3.13245

Everson J, Nelson HF, 1993. Rocket plume radiation base heating by reverse Monte Carlo simulation. *Journal of Thermophysics and Heat Transfer*, 7(4):717-723. https://doi.org/10.2514/3.482

Gao M, Guo XY, Zou MS, et al., 2015. Studies on combustion of aluminum-magnesium alloy hydro-reactive metal fuel. *Journal of Propulsion Technology*, 36(4):629-634 (in Chinese). https://doi.org/10.13675/j.cnki.tjjs.2015.04.021

Gao X, Yang QZ, Zhou H, et al., 2013. Numerical simulation on the infrared radiation characteristics of S-shaped nozzles. *Applied Mechanics and Materials*, 482:282-286. https://doi.org/10.4028/www.scientific.net/amm.482.282

Geisler-Moroder D, Dür A, 2010. A new ward BRDF model with bounded albedo. *Computer Graphics Forum*, 29(4): 1391-1398. https://doi.org/10.1111/j.1467-8659.2010.01735.x

Huang HS, Tong ZX, Chai SJ, et al., 2018. Experimental and numerical study of chaff cloud kinetic performance under impact of high speed airflow. *Chinese Journal of Aeronautics*, 31(11):2080-2092. https://doi.org/10.1016/j.cja.2018.08.002

Koch EC, Weiser V, Roth E, et al., 2011. Consideration of some 4*f*-metals as new flare fuels–europium, samarium, thulium and ytterbium. 42nd International Annual Conference of the Fraunhofer ICT. https://doi.org/10.13140/2.1.5156.3205

Lan T, Chen D, Chen SQ, et al., 2015. Implementation of adjoint/reverse Monte Carlo method in the analysis of satellites radiation. *Chinese Journal of Space Science*, 35(2):203-210 (in Chinese). https://doi.org/10.11728/cjss2015.02.203

Li ZH, Wang LS, 2009. Modeling study on holistic kinetic performance of chaff cloud. *Journal of System Simulation*, 21(4):928-931 (in Chinese). https://doi.org/10.16182/j.cnki.joss.2009.04.001

Liao YF, Cao YW, Wu SM, et al., 2016. Investigation into co-combustion characteristics of dyeing sludge and bituminous coal based on TGA-FTIR. *Journal of South China University of Technology (Natural Science Edition)*, 44(4):1-9 (in Chinese). https://doi.org/10.3969/j.issn.1000-565X.2016.04.001

Lin T, Li K, 2007. Research on a model of distributed surface type infrared decoy. *Electro-Optic Technology Application*, 22(1):72-74 (in Chinese). https://doi.org/10.3969/j.issn.1673-1255.2007.01.022

Lv MS, 2015. Approach jamming effectiveness evaluation for surface-type infrared decoy in network centric warship formation. AOPC 2015: Optical and Optoelectronic Sensing and Imaging Technology, Article 967423. https://doi.org/10.1117/12.2199842

Nebel JC, 1998. A new parallel algorithm provided by a numerical model. Second Eurographics Workshop on Parallel Graphics and Visualisation.

Nikodym T, 2010. Ray Tracing Algorithm for Interactive Applications. PhD Thesis, Czech Technical University in Prague, Prague, Czech Republic.

SAAB Technologies, 2017. BOL for F/A-18: Advanced Countermeasure Dispenser. https://saab.com/air/electronic-warfare/countermeasure-dispenser-systems/bol-fa-18/

Su PR, Eri Q, Wang Q, 2014. Optical roughness BRDF model for reverse Monte Carlo simulation of real material thermal radiation transfer. *Applied Optics*, 53(11):2324-2330. https://doi.org/10.1364/AO.53.002324

Sun W, Wang B, 2017. Calculation and image simulation of aircraft infrared radiation. *Laser & Infrared*, 47(6):728-735 (in Chinese). https://doi.org/10.3969/j.issn.1001-5078.2017.06.015

Tong Q, Li JX, Fang YW, et al., 2015. Simulation research on surface-type infrared decoy for jamming infrared imaging guided missile. *Infrared and Laser Engineering*, 44(4):

1150-1157 (in Chinese).
https://doi.org/10.3969/j.issn.1007-2276.2015.04.009

Viau CR, D'Agostino I, Cathala T, 2014. Coupling of TESS with SE-WORKBENCH for EO/IR countermeasure development and effectiveness assessment. 10th International IR Target and Background Modeling and Simulation (ITBM&S) Workshop, p.1-14.

Wang S, Mohan S, Dreizin EL, 2016. Effect of flow conditions on burn rates of metal particles. *Combustion and Flame*, 168:10-19.
https://doi.org/10.1016/j.combustflame.2016.03.014

Wang ZW, Ning HJ, Wang JL, et al., 2015. Simulation and analysis of plates cluster distribution of surface-type infrared decoy. *Acta Armamentarii*, 36(6):994-1000 (in Chinese).
https://doi.org/10.3969/j.issn.1000-1093.2015.06.005

Whitted T, 1979. An improved illumination model for shaded display. Proceedings of the 6th Annual Conference on Computer Graphics and Interactive Techniques, Article 14.
https://doi.org/10.1145/965103.807419

Wilharm CK, 2003. Combustion model for pyrophoric metal foils. *Propellants, Explosives, Pyrotechnics*, 28(6):296-300.
https://doi.org/10.1002/prep.200300031

Wu X, Zhang JQ, 2015. Signature simulation of infrared target by tracing multiple areal sources. *Applied Optics*, 54(13): 3842-3848.
https://doi.org/10.1364/AO.54.003842

Wu X, Zhang JQ, Chen Y, et al., 2015. Real-time mid-wavelength infrared scene rendering with a feasible BRDF model. *Infrared Physics & Technology*, 68:124-133.
https://doi.org/10.1016/j.infrared.2014.11.011

Yan CJ, Fan W, 2016. Combustion Science (3rd Edition). Northwestern Polytechnical University Press, Xi'an, China (in Chinese).

Yuan Y, Sun CM, Zhang XB, 2010. Measuring and modeling the spectral bidirectional reflection distribution function of space target's surface material. *Acta Physica Sinica*, 59(3):2097-2103 (in Chinese).
https://doi.org/10.7498/aps.59.2097

Zou T, Wang CZ, Tong ZX, et al., 2016. Diffusion rule of foil-surface-type infrared decoy. *Acta Aeronautica et Astronautica Sinica*, 37(9):2634-2645 (in Chinese).
https://doi.org/10.7527/S1000-6893.2016.0023

Appendix A: Parameters in Eq. (2) and reflection characteristics of chaffs

In Eq. (2), θ_i and θ_r are the incident and reflected angles, ϕ_i, ϕ_r, and ϕ_h are the azimuth angles for the incident, reflected, and halfway vectors, respectively, α and β are the roughness values equal to $\sqrt{2}$ times the standard deviations in the perpendicular directions of the 2D Gaussian distribution, ρ_s is the specular reflectance, and δ is the angle between the surface normal and the halfway vector.

If the azimuth angle ϕ_i=0, the specular reflectance ρ_s=1, the incident angle θ_i=0, π/8, π/6, and π/4, and the roughness values α=β=0.2 and 0.4, respectively, the values of probability obtained by the new Ward method f_{newWard} under different azimuth angles and pitch angles of reflected rays calculated according to Eq. (2) are shown in Figs. A1 and A2.

Appendix B: Deduction of Eq. (7)

If the midline vector in the cone of sight of the pixel point P_1 at $(0, y_1, z_1)$ is $\boldsymbol{n}$=(n_x, n_y, n_z), the equation of the spatial straight line is

$$\frac{x-x_1}{n_x}=\frac{y-y_1}{n_y}=\frac{z-z_1}{n_z},\quad n_x, n_y, n_z \neq 0. \tag{B1}$$

If sight lines of each pixel point distribute uniformly in the field of view of the infrared detector and y_m is the maximum y value of the focal plane array in the focal plane coordinate system, the included angle between point P_1 and the XOZ plane is

$$\frac{y_1}{y_m}\frac{\theta_1}{2}. \tag{B2}$$

Similarly, the included angle between point P_1 and the XOY plane is

$$\frac{z_1}{z_m}\frac{\theta_2}{2}. \tag{B3}$$

Therefore,

$$\begin{cases} n_y = n_x \tan\dfrac{\theta_1 y_1}{2y_m}, \\ n_z = n_x \tan\dfrac{\theta_2 z_1}{2z_m}. \end{cases} \tag{B4}$$

This equation brought into Eq. (B1) gives

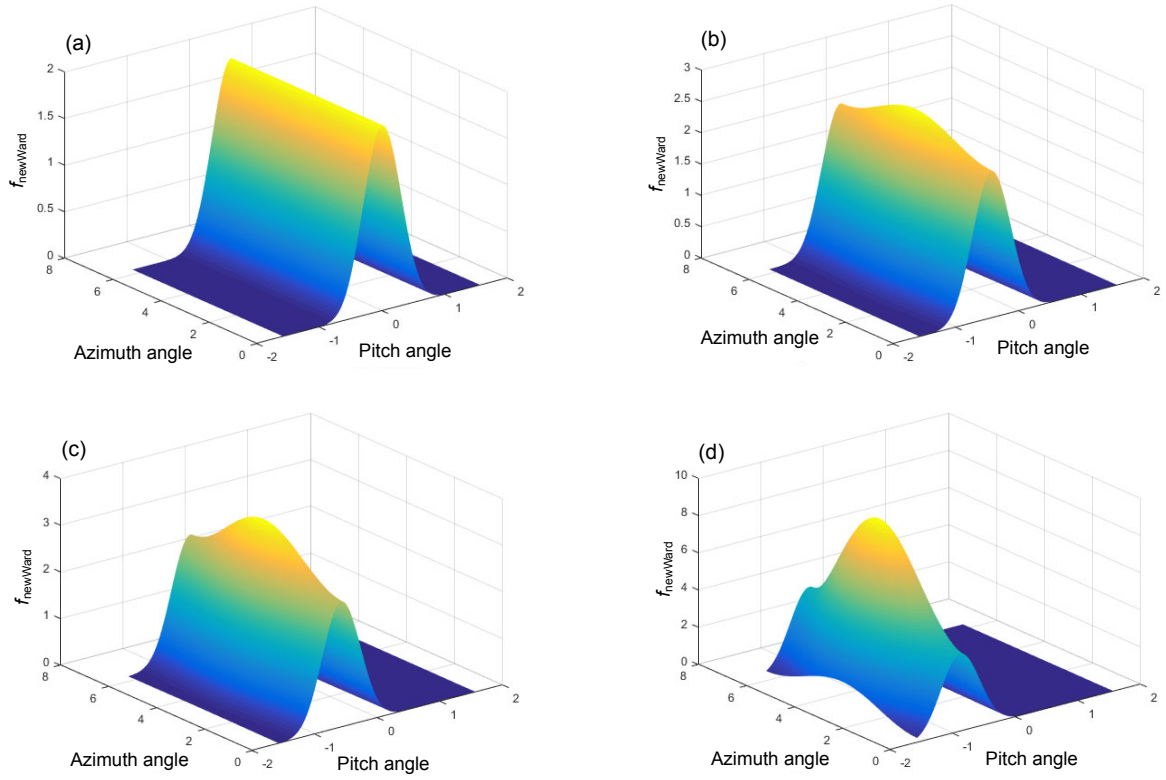

Fig. A1 $f_{newWard}$ under different azimuth and pitch angles (α=β=0.2): (a) θ_i=0; (b) θ_i=π/8; (c) θ_i=π/6; (d) θ_i=π/4

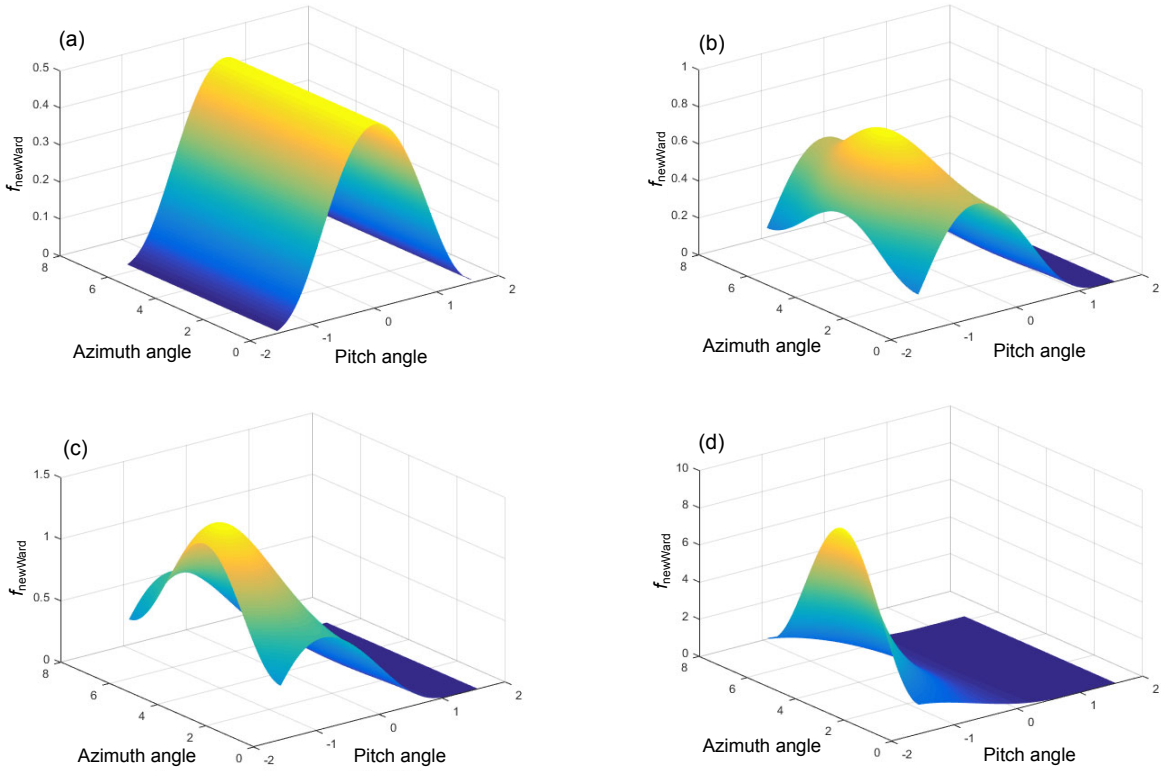

Fig. A2 $f_{newWard}$ under different azimuth and pitch angles (α=β=0.4): (a) θ_i=0; (b) θ_i=π/8; (c) θ_i=π/6; (d) θ_i=π/4

$$x-x_1=\frac{y-y_1}{\tan\dfrac{\theta_1 y_1}{2y_\mathrm{m}}}=\frac{z-z_1}{\tan\dfrac{\theta_2 z_1}{2z_\mathrm{m}}},\quad y_1,z_1\neq 0. \tag{B5}$$

When y_1=0, the sight lines are in the *XOZ* plane and the equation of the straight line can be expressed as

$$\begin{cases} x-x_1=\dfrac{z-z_1}{\tan\dfrac{\theta_2 z_1}{2z_\mathrm{m}}}, & z_1\neq 0,\\ y=0. \end{cases} \tag{B6}$$

Similarly, the equation of straight line z_1=0 is

$$\begin{cases} x-x_1=\dfrac{y-y_1}{\tan\dfrac{\theta_1 y_1}{2y_\mathrm{m}}}, & y_1\neq 0,\\ z=0. \end{cases} \tag{B7}$$

By combining Eqs. (B3)–(B5), the midline equation of the cone of sight for the pixel points at $(0, y_1, z_1)$ can be described as

$$\begin{cases} xy_1\tan\dfrac{\theta_1 y_1}{2y_\mathrm{m}}=y-y_1,\\ xz_1\tan\dfrac{\theta_2 z_1}{2z_\mathrm{m}}=z-z_1. \end{cases} \tag{B8}$$

中文概要

题　目： 高速气流作用下自燃箔片云团的辐射特性计算与实验研究

目　的： 当自燃箔片云团在空气中扩散时，自燃箔片云团之间存在大量的对辐射的遮挡、吸收和反射作用，并且箔片与空气之间也会发生相互作用，这使得辐射传输计算变得更加复杂。本文旨在计算自燃箔片云团的辐射特性并生成辐射图像。

创新点： 建立自燃箔片云团的辐射计算模型和燃烧模型，并得到辐射图像和光谱特性曲线。

方　法： 1. 针对辐射的传输特点，建立一种基于反向路径采样的辐射计算模型；该模型假设探测器按照辐射的反向均匀向外发射光线，采样统计各光线的路径后，正向计算探测器接收到的光线数量与强度。2. 考虑箔片表面的多孔结构对活性金属燃烧反应速率的影响并建立箔片的自燃模型；将计算结果与实验数据进行对比，验证该模型的准确性。3. 计算得到箔片云团的光谱分布并生成辐射图像。

结　论： 1. 箔片燃烧后温度迅速攀升，并在 1.3 s 左右达到最大值；随后，温度缓慢下降，并在 6 s 左右下降到接近环境温度。2. 箔条云扩散后呈椭圆形，扩散区随着时间的推移逐渐扩大，且亮度中心向后移动。3. 箔条云的光谱辐射强度极大点位于波长 1.4、1.9、3.1、4.3 和 8.0 μm 处，并且在 3.1 μm 时达到最大值。

关键词： 箔片云团；辐射计算；光谱辐射特性；活性金属；自燃